AO16: Detecting Sulfur Dioxide Emissions From Volcanoes Using the Infrared Atmospheric Sounding Interferometer

Ben Bradley

Supervisors: Dr I. A. Taylor and Prof. R. G. Grainger

Abstract

Real-time satellite detections of volcanic gases are crucial for alerting aviation to volcanic cloud hazards. A computationally fast algorithm, based on Walker et al. [1], was developed to detect volcanic clouds utilising the ν_1 absorption feature of sulfur dioxide (SO_2). The algorithm was then used to study the Nabro 2011 and Kelud 2014 volcanic eruptions, using spectral data from the Infrared Atmospheric Sounding Interferometer. The results were compared to an existing implementation of this algorithm, which instead makes use of the more strongly absorbing ν_3 feature. There was good agreement when high SO_2 concentrations were expected and before significant dispersion. The centres of volcanic clouds were well-identified throughout, though identification of the cloud edges became progressively worse. For both case studies, this allowed the presence and major structural features of volcanic clouds to be successfully identified for several days after emission. After this, the ν_1 algorithm became insensitive to large fractions of volcanic clouds, making it unsuited to studying evolution and dispersal over longer time frames.

1 Introduction

1.1 Background

Volcanic eruptions are violent geological events that often pose risks to people and infrastructure. Whilst many of these risks are confined to the area immediately surrounding a volcano, clouds of ash and gas can travel several thousand kilometres in the atmosphere.

The vulnerability of aircraft to volcanic ash [2] can necessitate airspace closure. This occurred during the 2010 eruption of Eyjafjallajökull, resulting in an estimated USD 1.7 billion in revenue losses [3]. Fine volcanic ash also constitutes a respiratory hazard, particularly to people with asthma or other pre-existing lung diseases [4].

When the volcanic gas sulfur dioxide (SO_2) is injected into the stratosphere, the sulfate aerosols it forms scatter light, increasing the albedo of the Earth. In extreme cases this results in a reduction in global temperatures of a degree or more over a timescale of years [5]. SO_2 and sulfate aerosols have also been shown to degrade aircraft components and necessitate costly repairs [6].

Detecting ash and SO_2 emissions from volcanoes is therefore critical for issuing informed warnings to the aviation industry and quantifying volcano-induced climate forcings. Methods that allow real-time detection of volcanic clouds are especially important for swift and informed responsive action to be taken.

1.2 Infrared Remote Sensing of SO_2

The Infrared Atmospheric Sounding Interferometer (IASI) satellite instrument provides global, high spectral resolution data which can be used to detect atmospheric SO_2 and locate volcanic clouds. Unlike ultraviolet and visible remote sensing, infrared data can be collected during the night, allowing uninterrupted monitoring. Normally present in the atmosphere in trace quantities, the elevated SO_2 concentrations found in volcanic clouds are relatively easy to identify and track.

Whilst ash is of primary concern to aviation, there are several challenges to detecting it directly. These include ice and overlying clouds obscuring the spectral signal, false positives from water-rich clouds, and poor thermal contrast to the underlying terrain [7]. SO_2 can be used as a proxy for ash, though this assumption should be used cautiously since separation can occur due to lifetime and wind shear effects [8].

SO_2 concentrations are measured using total column amounts, which quantify the number of SO_2 molecules within a vertical column of atmosphere. These can be estimated from IASI spectral data by means of a fast SO_2 linear retrieval algorithm, described in Walker et al. [1]. This algorithm, hereafter called the linear retrieval, utilises all the channels surrounding an SO_2 absorption feature, providing greater sensitivity than other methods that use a select few. It is computationally fast as it assumes linearity between the measured strength of SO_2 absorption features and the SO_2 column amount. Due to this simplifying assumption, the column amounts returned should only be used as an indicator of el-

evated concentrations. For accurate estimates, iterative algorithms initialised by the linear retrieval can be used [9].

1.3 SO$_2$ Absorption Features

Within IASI's spectral range there are three SO$_2$ absorption features, described in table 1. The strongest feature, ν_3, is utilised in an existing linear retrieval for IASI that has been in use for over a decade [9]. It is generally the most sensitive feature to SO$_2$, though it overlaps areas of strong absorption from water vapour, limiting its sensitivity at low altitudes. The ν_1 feature is located in an atmospheric window, preventing these water absorption features from obscuring the spectral signal. This allows sensitivity to be maintained down to the Earth's surface and low-altitude emissions to be detected. Unfortunately, it overlaps spectral signatures from clouds and volcanic ash, which can obscure the signal from SO$_2$. Strong reflections with high spectral dependence from quartz (known as quartz Reststrahlen) can also cause problems over arid regions unless specifically accounted for in the linear retrieval implementation [10]. The $\nu_1 + \nu_3$ feature is only of use when other features are saturated [11] and is not considered in this study.

Table 1: Infrared absorption features of SO$_2$ [9].

Name	Central Wavelength	Comments
ν_1	$8.7\,\mu$m	Focus of report
ν_3	$7.3\,\mu$m	Strongest
$\nu_1 + \nu_3$	$4.0\,\mu$m	Weakest

The Infra-Red Sounder (IRS) satellite instrument, due for launch in spring 2025, has a spectral range that includes the ν_1 feature but not the currently used ν_3 feature. IRS will be positioned in a 0° longitude geostationary orbit, providing coverage over Europe every 30 minutes and 3–6 times every 6 hours for other disc locations [12]. This temporal resolution is a considerable improvement on the two daily scans possible from polar-orbiting instruments such as IASI. Furthermore, its high spectral resolution vastly outperforms the existing European geostationary infrared satellite instrument (the Spinning Enhanced Visible Infra-Red Imager) which has only 12 spectral channels [13]. These improvements in temporal and spectral resolution could allow faster detections and warnings for volcanic clouds over Europe and Africa. This strongly motivates the development of a ν_1 linear retrieval, despite the expected reduction in sensitivity. As an infrared instrument with comparable spectral resolution, IASI data provides a useful test for the performance of this algorithm.

This report describes the development of a fast SO$_2$ linear retrieval algorithm, applied to IASI spectral data surrounding the ν_1 infrared absorption feature. The specifications of the IASI instrument are described in section 2.1. An overview of the linear retrieval and derivation of its fundamental equations is given in section 2.2. Descriptions of the spectral ensembles, flagging protocols, and performance metrics required then follow in sections 2.3, 2.4, and 2.5. Computational speed and threshold determination are discussed in section 3.1. The ν_1 linear retrieval is applied to eruption case studies of Nabro (Eritrea) 2011 and Kelud (Indonesia) 2014 in sections 3.2 and 3.3, where the results are compared to those of the existing ν_3 linear retrieval. By characterising the strengths and deficiencies of the ν_1 linear retrieval, its ability to detect volcanic clouds from major eruptions is assessed.

2 Method

2.1 The IASI Satellite Instrument

IASI is a Fourier transform spectrometer with a spectral range of 645–2760 cm^{-1} and channel spacing of 0.25 cm^{-1}. Scans are ±48.3° of nadir, giving a 2200 km swath width. Each circular pixel has a 12 km diameter at nadir; rows of 2×2 pixel groups form each swath [14]. The EUMETSAT MetOp satellites that carry IASI instruments are in sun-synchronous polar orbits, achieving near-global coverage every 12 hours. There are three instruments: IASI-A (2006–2021); IASI-B (2012–); and IASI-C (2018–). Data from IASI-A was used in this study, though it would be easy to utilise data from the other IASI instruments.

2.2 The Linear Retrieval Algorithm

2.2.1 Summary

IASI provides spectral radiance measurements as Brightness Temperatures (BT) in units of Kelvin. The linear retrieval algorithm described in Walker et al. [1] exploits the high spectral resolution of this data, with all channels surrounding an SO$_2$ absorption feature utilised. Comparison between channels inside and outside the chosen absorption feature fixes the spectral background, allowing the reductions in BT from the SO$_2$ absorption feature to be extracted. By assuming column amounts increase linearly with reductions in BT, data from all the spectral channels under consideration is combined to form an optimal estimate of the SO$_2$ column amount. This algorithm was implemented using the programming language Python and is described below.

2.2.2 Output and Inputs

Detailed here are the inputs required by the linear retrieval and its output. A description and origin for each parameter are listed below, with a summary provided in table 2.

The output is the total column amount of SO_2 in Dobson Units (DU). This measures the number of SO_2 molecules within a vertical column of atmosphere. $1\,DU = 2.69 \times 10^{20}$ molecules m^{-2}. The scalar x gives its value at a chosen pixel.

Spectral radiance measurements from IASI form the primary input. These measurements are specific to the pixel being processed, unlike other inputs which remain the same for all applications of the linear retrieval. The spectral measurements for all n wavenumber channels under consideration are gathered within the spectral vector $\mathbf{y} \in \mathbb{R}^n$. In this case, channels in and around the ν_1 absorption feature from 1000–1200 cm^{-1} were considered, resulting in $n = 801$ channels.

The total column amount of SO_2 under standard atmospheric conditions x_0 was found using pressure and SO_2 concentration data from an equatorial atmospheric sounding. This climatological value was calculated to be $0.0767\,DU$ by integrating the concentration measurements through a column of atmosphere, as described in appendix A.

The atmospheric sounding data was perturbed and the resulting spectral measurements simulated using the Reference Forward Model, a radiative transport model described in Dudhia [15]. The behaviour of each y_i within $\mathbf{y}$ in response to a change in column amount around x_0 was captured in the Jacobian $\mathbf{k} \in \mathbb{R}^n$, the ith entry of which is $\frac{dy_i}{dx}$.

A large ensemble of spectra from pixels experiencing normal atmospheric (climatological) concentrations of SO_2 was used to calculate the ensemble parameters $\mathbf{y}_0$ and $\mathbf{S}_\epsilon$. The climatological spectral vector $\mathbf{y}_0 \in \mathbb{R}^n$ represents the mean BT measurements under these conditions. The covariance matrix $\mathbf{S}_\epsilon \in \mathbb{R}^{n \times n}$ contains the joint variability between any two elements of the spectral vector $\mathbf{y}$. This is crucial for incorporating the random and systematic errors of the spectral measurements into an optimal unconstrained least squares estimate of x. Further details on the spectral ensemble are discussed in section 2.3.

2.2.3 Linear Retrieval Calculation

Under an assumption of linearity, these parameters are drawn together to construct the relation

$$\mathbf{y} - \mathbf{y}_0 = (x - x_0)\,\mathbf{k} + \epsilon_{\text{rnd}} + \epsilon_{\text{sys}} \qquad (1)$$

where the random and systematic errors have been explicitly included as ϵ_{rnd} and ϵ_{sys} respectively.

The covariance matrix characterising these errors is then used to provide an optimal unconstrained least-squares estimate of x:

$$x = x_0 + \left(\mathbf{k}^T\,\mathbf{S}_\epsilon^{-1}\,\mathbf{k}\right)^{-1} \mathbf{k}^T\,\mathbf{S}_\epsilon^{-1}\,(\mathbf{y} - \mathbf{y}_0). \qquad (2)$$

For the purpose of computational efficiency, the linear retrieval was run simultaneously for a large number of pixels. The matrix techniques used are noted in Smith [16] and described in appendix B.

2.3 The Spectral Ensemble

2.3.1 Summary

A large ensemble of N spectra experiencing standard atmospheric concentrations of SO_2 is required for calculating the climatological spectral vector $\mathbf{y}_0$ and covariance matrix $\mathbf{S}_\epsilon$. When running the linear retrieval, these ensemble parameters allow SO_2 absorption to be separated from the spectral background, without needing to identify and subtract the contributions from all local climatic parameters. A first estimate for the spectral vector is provided by $\mathbf{y}_0$, around which perturbations are measured. The covariance matrix then provides a weighting to each spectral channel's contribution to the estimate of x, based on the systematic and random errors associated with that channel. Systematic errors arise from variability in climatic parameters (e.g. temperature, cloudiness, interfering species) within the ensemble. Random errors are associated with the instrument noise and are included in the covariance because climatological SO_2 levels generate signals significantly smaller than this noise.

2.3.2 Ensemble Parameter Calculations

Consider an ensemble of N spectra (each denoted $\mathbf{y}_j$ for $1 \leq j \leq N$) contained within a spectral matrix $\mathbf{Y} \in \mathbb{R}^{n \times N}$. Averaging the spectra in the ensemble provides an estimate for $\mathbf{y}_0$:

$$\mathbf{y}_0 \approx \bar{\mathbf{y}} = \frac{1}{N}\sum_{j=1}^{N} \mathbf{y}_j. \qquad (3)$$

The covariance matrix $\mathbf{S}_\epsilon$ is given by equation (4), which can also be expressed using the spectral matrix $\mathbf{Y}$ in equation (5).

$$\mathbf{S}_\epsilon = \frac{1}{N-1}\sum_{j=1}^{N}\left(\mathbf{y}_j - \bar{\mathbf{y}}\right)\left(\mathbf{y}_j - \bar{\mathbf{y}}\right)^T \qquad (4)$$

$$= \frac{1}{N-1}\left(\mathbf{Y} - \bar{\mathbf{y}}\left(\mathbf{1}^N\right)^T\right)\left(\mathbf{Y} - \bar{\mathbf{y}}\left(\mathbf{1}^N\right)^T\right)^T \qquad (5)$$

Table 2: A summary of the output and input parameters used by the linear retrieval. The dimension n is the number of spectral channels under consideration, which was $n = 801$ for the ν_1 linear retrieval.

Name	Symbol	Source	Unit	Dimension
SO$_2$ column amount estimate	x	Linear retrieval output	DU	Scalar
BT spectral measurement vector	$\mathbf{y}$	IASI	K	n
Climatological SO$_2$ column amount	x_0	Atmospheric sounding	DU	Scalar
Jacobian	$\mathbf{k}$	Reference Forward Model	K DU^{-1}	n
Climatological spectral vector	$\mathbf{y}_0$	Spectral ensemble	K	n
Covariance matrix	$\mathbf{S}_\epsilon$	Spectral ensemble	K^2	$n \times n$

Here $\mathbf{1}^N$ is defined to be an N-dimensional vector for which every entry is unity. Multiplying this expression out, noting that $\mathbf{Y1}^N = N\bar{\mathbf{y}}$ and $\left(\mathbf{1}^N\right)^T \mathbf{1}^N = N$ yields

$$\mathbf{S}_\epsilon = \frac{1}{N-1}\left(\mathbf{YY}^T - N\bar{\mathbf{y}}\bar{\mathbf{y}}^T\right). \qquad (6)$$

As noted by Smith [16], the linearity of the terms $\mathbf{YY}^T$ and $\bar{\mathbf{y}}$ can be exploited when computing the ensemble parameters. For details, see appendix C.

2.3.3 Ensemble Construction

Spectral ensembles were constructed from one month of IASI-A data for each eruption case study, as summarised in table 3. Although reasonable results can be obtained globally using any ensemble, the month and location were matched as closely as possible to those of the case study to ensure the most accurate estimates. If the ensemble is constructed over non-arid regions, the effects of quartz Reststrahlen will not be captured. In this case, the ν_1 linear retrieval will output negative column amounts over arid regions.

To be sure the ensembles contained non-elevated SO$_2$ concentrations, proposed months and areas were checked using the ν_3 linear retrieval. In each instance, the number of spectra with elevated concentrations of SO$_2$ constituted less than 0.005% of the total ensemble, providing confidence that climatological conditions were represented. The ν_3 linear retrieval uses a spectral ensemble constructed over the Atlantic Ocean [10].

2.4 Flagging Threshold

The SO$_2$ column amount x returned by the linear retrieval should only be used as an indicator of elevated SO$_2$ concentrations. As such, a threshold must be established to determine when column amounts can be distinguished from background noise and be considered elevated. Pixels above this value can then be flagged and separated from the non-flagged pixels.

2.4.1 Flagging Protocol for ν_3

Under climatological conditions, total column amounts can be approximated to a Gaussian distribution centred at x_0. The column amount standard deviation σ under these conditions is calculated using the covariance matrix and Jacobian:

$$\sigma = \left(\mathbf{k}^T\mathbf{S}_\epsilon^{-1}\mathbf{k}\right)^{-\frac{1}{2}}. \qquad (7)$$

This can be used to set a flagging threshold x_{thresh}:

$$x_{\text{thresh}} = x_0 + Z\sigma \qquad (8)$$

where Z is a chosen number of standard deviations from x_0. The ν_3 linear retrieval takes $Z = 5.1993$, resulting in a threshold of 0.4909 DU [10]. This corresponds to a false positive detection once per 10 million pixels processed if the background distribution is perfectly Gaussian. This provided high confidence these flagged pixels corresponded to true signatures and not random noise.

2.4.2 Flagging Protocol for ν_1

Standard deviations for the ν_1 spectral ensembles used to study Nabro and Kelud are given in table 3. These result in large thresholds of 6.31 DU and 7.05 DU under the ν_3 flagging protocol: suitable only for detecting the centre of volcanic clouds shortly after an SO$_2$-rich eruption. To adequately flag volcanic clouds using the ν_1 feature, a lower threshold was calculated using a more lenient flagging protocol.

By assuming the ν_3 linear retrieval flagged all instances of elevated SO$_2$ and all flagged pixels corresponded to genuine detections (i.e. perfect sensitivity and specificity), it was possible to validate the performance of the ν_1 linear retrieval. Based on this validation, an "optimal threshold" for ν_1 could then be selected. As with any detection method, the ν_3 linear retrieval has imperfect specificity and sensitivity (especially at low altitudes), but these assumptions were deemed reasonable in the context of volcanic cloud detection. Because the ν_1 feature is sensitive down to the surface, pixel location impacted the noise level encountered and it was useful

Table 3: Spectral ensembles used to calculate the covariance matrix and climatological spectral vector for the ν_1 linear retrieval. The % Flagged column shows the fraction of these spectra that were flagged by the ν_3 linear retrieval.

Case Study	Month	Latitude	Longitude	# Spectra N	% Flagged	Std. dev. σ
Nabro	Feb 2012	5°N–25°N	10°W–80°E	1,010,578	0.0048%	1.198 DU
Kelud	Mar 2013	40°S–5°N	60°E–150°E	2,274,407	0.0032%	1.341 DU

to adapt to this with different thresholds. A disadvantage of this method was its reliance on ν_3 linear retrieval validation data. If this were unavailable, an alternative method would be to adapt the ν_3 flagging protocol by using a smaller Z value.

The ν_1 linear retrieval performance at a given threshold was evaluated using a skill score formula. This methodology has previously been used in studies classifying cloud and dust presence [17], [18]. To best measure the ability to detect SO_2 and avoid false detections, a modified version of the True Test Score (TSS) was used, given by equation (9). A summary of the parameters used and their corresponding binary classifications is given in table 4.

A weighting parameter w was introduced to control the relative importance of maximising true positive detections and avoiding false negatives. Smaller w values result in smaller optimal thresholds and greater sensitivity, whereas larger values have larger optimal thresholds and fewer false positives. Choosing this weighting was somewhat subjective, but $w > 1$ was generally required. This was because smaller thresholds increased the number of genuine detections but also uniformly increased random noise. Artificially low thresholds were then favoured when $w \leq 1$, due to a large fraction of "true positive" classifications actually originating from random noise located in volcanic clouds. After a suitable weighting was chosen, the threshold that maximised the TSS was deemed "optimal" and was used to visualise the results.

$$\text{TSS} = \left(\frac{h}{h+u} - \frac{wf}{f+z} \right) \times 100 \qquad (9)$$

Table 4: Parameters within the modified TSS equation.

	Description	Classification
h	Flagged by ν_1 and ν_3	True positives
u	Flagged by ν_1 only	False positives
f	Flagged by ν_3 only	False negatives
z	Flagged by neither	True negatives
w	Weighting parameter	

2.5 Hit Rate

Once a suitable threshold was determined, a measure of the ν_1 linear retrieval's ability to detect volcanic clouds was needed. As before in section 2.4.2,

assumptions of perfect sensitivity and specificity allow the ν_3 results to be used as *a priori* indicators of elevated SO_2. A Hit Rate (HR) —the percentage of pixels containing elevated SO_2 that were correctly flagged by the ν_1 linear retrieval— can then be calculated using the h and u parameters within table 4, as given by equation (10). Whilst this is not a perfect measure of the ν_1 linear retrieval performance, it is a good indicator that can be easily evaluated for each orbit.

$$\text{HR} = \frac{h}{h+u} \times 100 \qquad (10)$$

3 Results and Analysis

3.1 Speed and Threshold Determination

Before running the ν_1 linear retrieval, the Jacobian $\mathbf{k}$, climatological column amount x_0, climatological spectral vector $\mathbf{y}_0$, and covariance matrix $\mathbf{S}_\epsilon$ were calculated. Processing times were seconds–minutes for $\mathbf{k}$ and x_0. Depending on the ensemble size, 2–4 hours were needed to determine $\mathbf{y}_0$ and $\mathbf{S}_\epsilon$.

The ν_1 linear retrieval, run on the JASMIN supercomputer, processed IASI-A data for all longitudes within the latitude range 70°S–70°N for the days following the Nabro 2011 and Kelud 2014 eruptions. Average processing times were ~ 5.6 ms per spectra or ~ 7 minutes per orbit. This speed is similar to that of the ν_3 linear retrieval [19].

Using the ν_1 flagging protocol described in section 2.4.2, "optimal thresholds" for several choices of weighting factor w were calculated using data from the first three days volcanic clouds were visible. After visualising the ν_1 linear retrieval results under these thresholds, it was found that for both case studies the choice $w = 5$ gave a suitable balance between sensitivity and specificity. For more details, see appendix D. The "optimal thresholds" under this choice of w are summarised in table 5. Also given are the resulting number of standard deviations Z from x_0 and the fraction f_Z of pixels expected to be above threshold due to random noise.

3.2 Nabro 2011 Case Study

Nabro is a volcano in Eritrea, close to the border of Ethiopia. Previously thought to be inactive, the

Table 5: The thresholds used by the linear retrievals.

Case Study	w	x_{thresh}	Z	f_Z
ν_1 Nabro	5	3.54 DU	2.89	1.9×10^{-3}
ν_1 Kelud	5	2.80 DU	2.03	2.1×10^{-2}
ν_3	–	0.49 DU	5.20	1.0×10^{-7}

volcano began erupting on the 12$^{\text{th}}$ June 2011. The large SO_2-rich volcanic clouds generated contained a maximum SO_2 loading of 1.6 ± 0.3 Tg but comparatively small volumes of ash [20]. This made the eruption ideal for studying the performance of the linear retrieval without significant impact from the ash absorption features that overlap the ν_1 band. The ability of the covariance matrix to suppress quartz Reststrahlen over arid regions was also investigated since the centre of the cloud travelled over the Sahara desert.

3.2.1 Volcanic Cloud Analysis

The pixels flagged by the ν_1 and ν_3 linear retrievals between the 13$^{\text{th}}$ and 18$^{\text{th}}$ June 2014 are shown in figure 1. The occasional gaps in the data are due to the viewing angles and orbit of IASI, which prevent full ground coverage when close to the equator. The volcanic cloud travels northwest from Nabro, covering Egypt. It then travels northeast before dispersing over Asia. The volcano is seen to continuously erupt over this period.

For each image in figure 1, the hit rate of the ν_1 linear retrieval is calculated, as seen in figure 2. This is defined as the percentage of the pixels flagged by ν_3 that were also flagged by ν_1, as given by equation (10). On the 13$^{\text{th}}$ June when the volcanic cloud is small, the data is filtered to exclude dispersed ν_3 detections not connected to the eruption that would otherwise skew the results. For later days the clouds are large enough for this not to be an issue. The hit rate for the total area imaged gradually decreases from a maximum of $\sim 80\%$ at the beginning of the eruption to $\sim 30\%$ as the volcanic cloud disperses. Strong agreement between the linear retrievals is seen in the centre of volcanic clouds, particularly when close to the volcano. Pixels flagged only by ν_3 occur primarily at the fringes of the clouds, where reduced SO_2 column amounts are not flagged due to the larger ν_1 threshold. This results in the main body and structure of the volcanic clouds being well-identified, but the edges of the cloud being poorly constrained. The hit rate of pixels within the Sahara is analysed in section 3.2.2.

Under a Gaussian distribution with $\sigma = 1.198$ DU, 0.19% of background data would be expected to exceed the 3.54 DU ν_1 threshold, corresponding to approximately 250 pixels per image. Since the number of pixels flagged only by ν_1 is closer to 800 per image, a considerable fraction is likely due to genuine low-altitude emissions that were not flagged by the ν_3 linear retrieval. Either way, the majority of these pixels are scattered across the image and do not appear to be part of the volcanic cloud structure. This so-called "salt and pepper" noise could be reduced by taking a larger weighting parameter w and thus a larger threshold, but this would reduce the sensitivity of the ν_1 linear retrieval. An avenue for further work is to construct a filtering algorithm that uses the number of neighbouring flagged pixels to remove this noise whilst maintaining the sensitivity.

3.2.2 The Impact of Quartz Reststrahlen

If not properly accounted for in the ν_1 covariance matrix, spectral reflections from quartz over arid regions cause negative offsets to SO_2 column amounts. The ν_1 linear retrieval's performance over the Sahara is compared to its performance over the total image in figure 2. The orange line shows the hit rates for pixels within the latitude, longitude limits 15°N–30°N, 0°E–30°E. For the 13$^{\text{th}}$–14$^{\text{th}}$ June these track well with the total performance, but after this the Sahara hit rate drops to 20% below that of the total image hit rate and does not recover. This indicates negative offsets to SO_2 column amounts from quartz Reststrahlen remain, resulting in a smaller proportion of pixels above the ν_1 threshold and a lower hit rate over the Sahara. High SO_2 column amounts prevent this from being relevant near the beginning of the eruption, but as the volcanic cloud disperses the negative offsets force some pixels below the ν_1 threshold.

Despite using a spectral ensemble that included arid regions, it can be concluded that the quartz Reststrahlen have not been fully suppressed. For more accurate detections over arid regions, an alternative method could be to process them separately, using a specially designed spectral ensemble. Such an ensemble should take a smaller sampling area and longer sample time to account for the quartz features more accurately.

3.2.3 Other Features

Since the ν_1 feature lies within an atmospheric window, some of the pixels flagged only by the ν_1 linear retrieval correspond to true surface-level signals that are impossible to detect using the ν_3 linear retrieval. A persistent SO_2 signal has previously been identified in Tunisia [21] and can be seen in figure 1 from the recurring ν_1 flags around (34°N, 8°E).
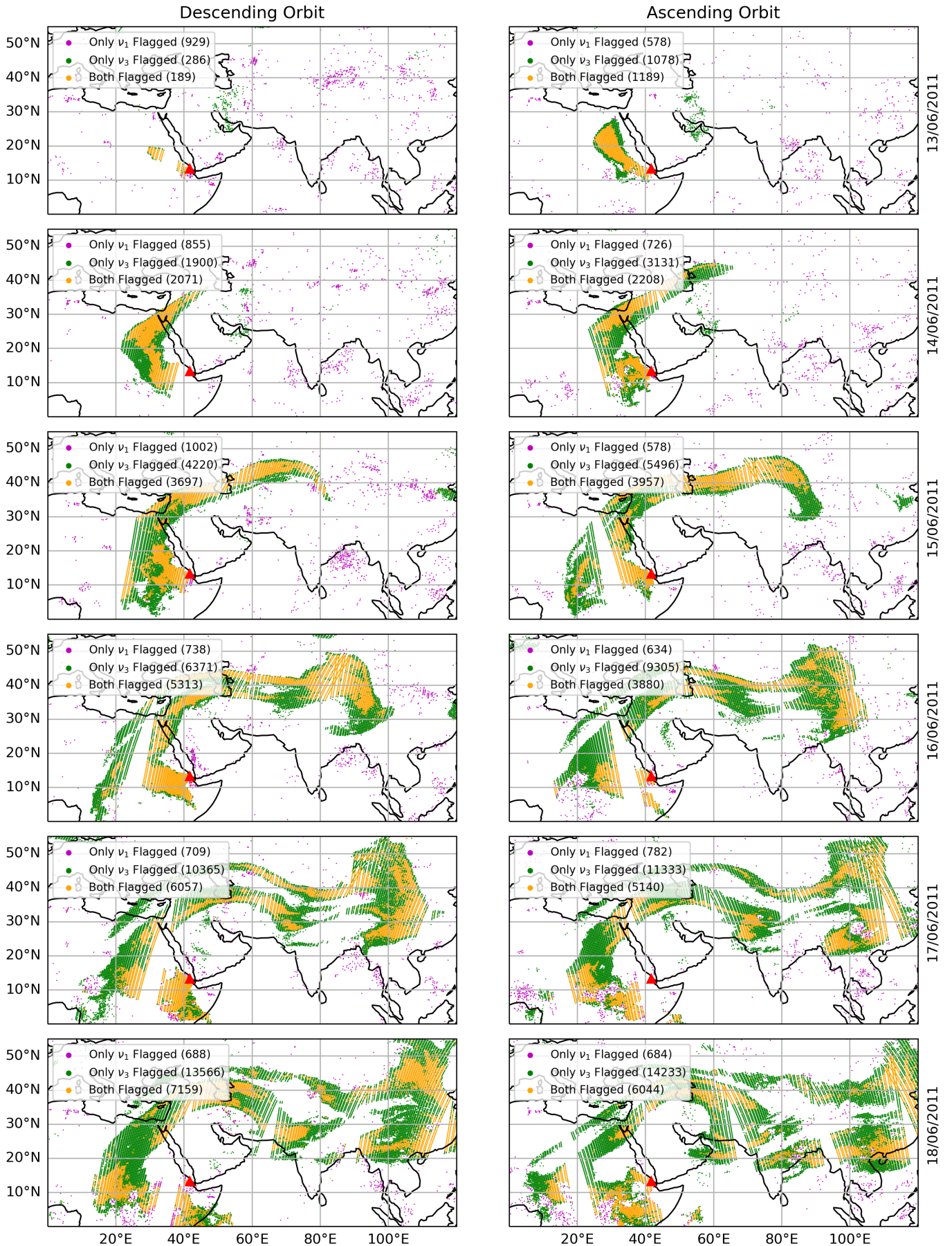
Figure 1: Comparison between pixels flagged by the ν_1 linear retrieval (purple and orange pixels, $x_{\text{thresh}} = 3.54 \, \text{DU}$) and the ν_3 linear retrieval (green and orange pixels, $x_{\text{thresh}} = 0.4909 \, \text{DU}$). The number of pixels corresponding to each category is given in the legend of each image. IASI-A data for the first six days of the Nabro 2011 eruption is shown. Each day has data from descending and ascending orbits, gathered at approximately 9:30 am and 9:30 pm (local time) respectively. The volcano location is displayed as a red triangle.
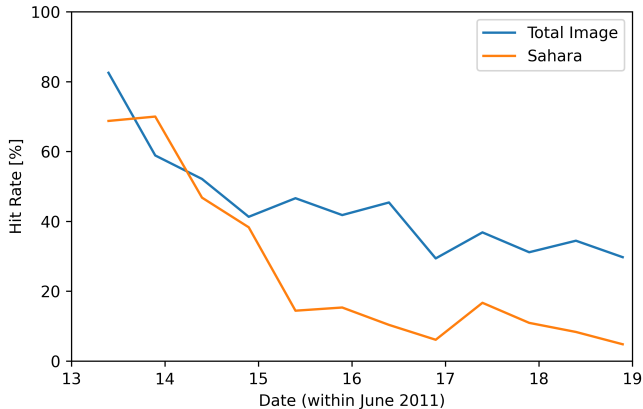
Figure 2: The hit rates calculated using equation (10) for each image within figure 1. Data is taken from pixels flagged within the total image (blue) and a subsection of the image over the Sahara (orange).

This source was also identified in [10]. Other persistent sources can be seen, the most notable at (45°N, 60°E) in Uzbekistan/Kazakhstan. Flagged pixels can be observed around the Persian Gulf, particularly on 17th and 18th June. Although there are few pixels flagged, they appear to follow the coastline, making them unlikely to be due to random noise. Many oil refineries in this area process sulfur-rich "sour" crude oil (e.g. Dubai Crude [22]). Loose clusters of detections around populous areas of China and India may also be linked to industrial activity, though this is less clear-cut. A study spanning a longer duration is recommended, where long-term averages can be used to verify the presence and persistence of these sulfur sources.

3.3 Kelud 2014 Case Study

Kelud (also commonly named Kelut) is a volcano in Indonesia, on the island of Java. Between the 13th and 15th February 2014 it erupted explosively, injecting volcanic ash and gas to altitudes of 16–17 km [23]. This case study assesses the performance of the ν_1 linear retrieval under conditions with a significant ash presence.

3.3.1 Volcanic Cloud Analysis

Comparisons between the pixels flagged by the ν_1 and ν_3 linear retrievals between the 14th and 17th February 2014 are shown in figure 4. As with the Nabro case study, there are occasional gaps due to limited coverage from IASI near the equator. The eruption began at approximately 22:30 local time on 13th February. The volcanic cloud emerges on the 14th, travelling southwest. A limb then detaches from the main body and drifts southeast, dispersing over Southern Australia. The eruption ends on the 15th. On the 16th, part of the cloud sur-

rounding the volcano begins travelling northeast.

The hit rates for each image in figure 4 are calculated and displayed in figure 3. A similar trend is observed to that of the Nabro eruption, with hit rates $> 50\%$ early in the eruption gradually decreasing, in this case to $\sim 20\%$. Hit rates are generally slightly lower than those of Nabro despite a lower threshold being used, though this is not unsurprising given the extreme amounts of SO_2 injected by Nabro and its longer eruptive period. The cloud that begins travelling Northeast on the 16th has very few pixels flagged by the ν_1 linear retrieval, as does the limb travelling over Southern Australia. The inability to detect the dispersing limbs of the volcanic cloud suggests the ν_1 linear retrieval is poorly suited for monitoring SO_2 for longer than a few days after its injection into the atmosphere.
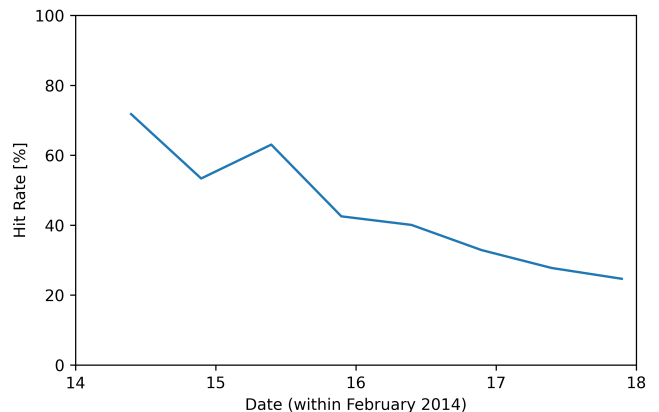

Figure 3: The hit rates calculated using equation (10) for each image within figure 4.

Under a Gaussian distribution with $\sigma = 1.341\,\mathrm{DU}$, 2.1% of background data would be expected to exceed the $2.80\,\mathrm{DU}$ ν_1 threshold, corresponding to approximately 1400 pixels per image. This is close to the number of pixels flagged only by ν_1, suggesting most correspond to random noise.

4 Conclusion

An SO_2 linear retrieval algorithm using the ν_1 absorption feature was developed and applied to eruption case studies of Nabro 2011 and Kelud 2014. Processing times were measured at ~ 7 minutes per orbit, allowing real-time applications of this method. The percentages of pixels flagged by the existing ν_3 linear retrieval that were also flagged by the ν_1 linear retrieval were measured. These were $> 50\%$ for the first 1–2 days imaged but gradually decreased to 20–40% as the volcanic clouds dispersed and column amounts dropped below the threshold, as seen in figures 2 and 3. In both case studies, the ν_1 linear retrieval struggled to detect the fringes and finer dispersion structures of the
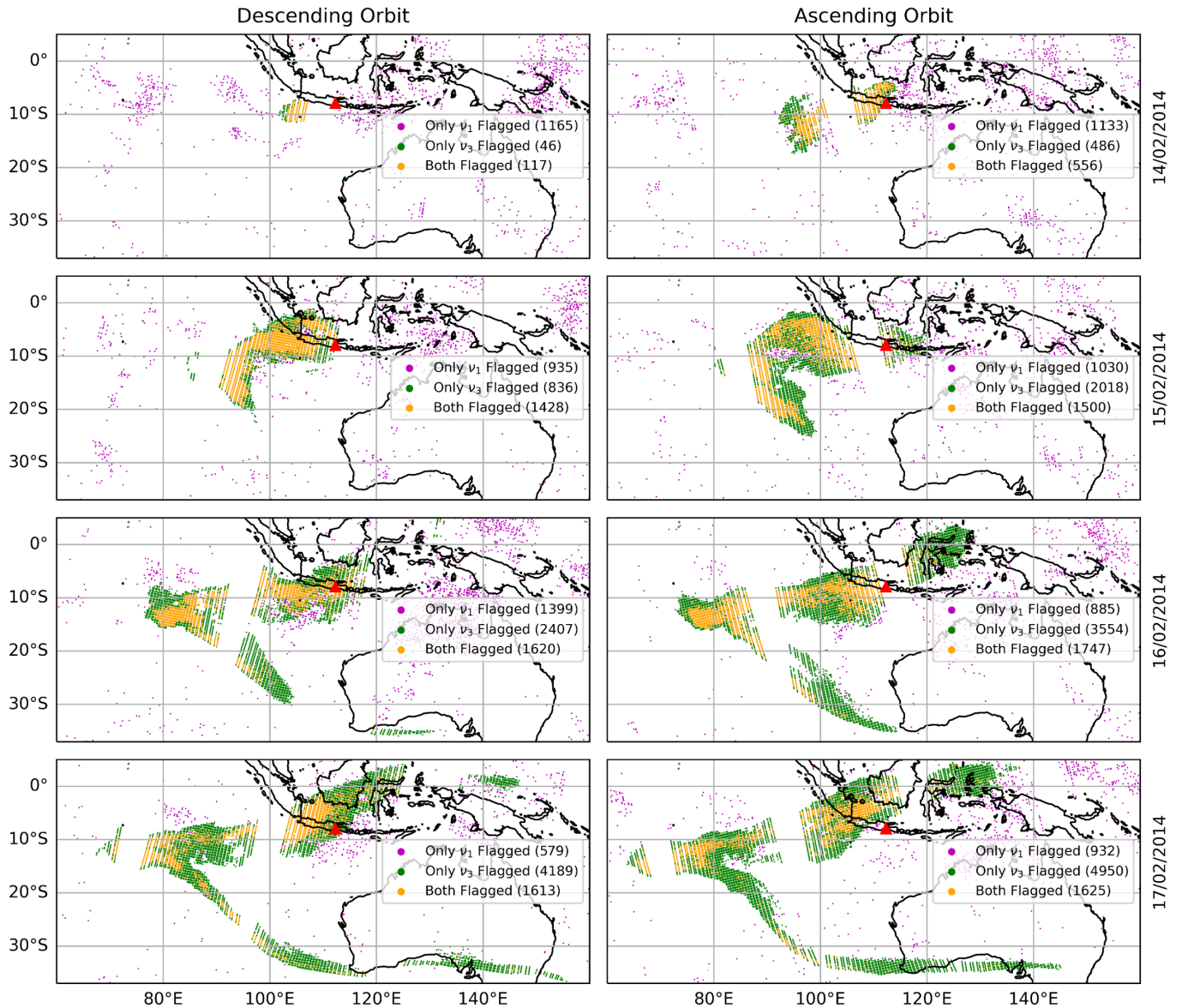
Figure 4: The same as figure 1 but with data pertaining to the first four days of the Kelud 2014 eruption. The ν_1 threshold used is 2.80 DU; the ν_3 threshold remains 0.4909 DU.

clouds. It also struggled to flag pixels over Saharan regions in the Nabro study, with percentages after the 15th of June reaching only 5–20%, likely due to interfering spectral features from exposed quartz. This was in spite of efforts to incorporate them into the spectral ensemble. Despite the limitations of the ν_1 linear retrieval compared to its ν_3 counterpart, figures 1 and 4 show success in identifying the presence and main structure of volcanic clouds from major eruptions. There was good sensitivity to SO_2 soon after emission, such as in areas surrounding the volcanoes while they were erupting and during the first 1–2 days, with reasonable sensitivity several days following this. These results suggest the ν_1 linear retrieval is suited to initial volcanic hazard monitoring but unsuited to long-term dispersal studies or monitoring small-scale volcanic activity. The potential to adapt the method to process data from the upcoming IRS instrument should make this work of interest to Volcanic Ash Advisory Centers that monitor volcanic hazards to aviation. It would allow high spectral resolution measurements of SO_2 to be made with significantly improved temporal resolution.

Further testing of the ν_1 linear retrieval is suggested for weaker eruptions and the latter stages of major eruptions to establish when the technique becomes fully insensitive to volcanic clouds. Additionally, comparisons of the SO_2 column amount outputs to those of iterative algorithms would allow the output accuracy to be quantified. To combat the random "salt and pepper" noise present in the results, a filter that removes isolated flagged pixels not part of a larger cloud structure could be developed. Another avenue of future work is investigating the optimal number of spectra needed for the spectral ensemble. Knowledge of the spatial and temporal dependence of these ensembles would also

aid their construction. When viewing arid regions, the effects of quartz Reststrahlen were apparent, reducing sensitivity to SO_2 (figure 2). A specifically designed ensemble could be constructed to better account for the impact of these quartz features. Such an ensemble would require a smaller sample area and a sample time larger than one month and could then be used for processing spectra from predefined arid regions. The low-altitude sensitivity of the ν_1 feature allowed potential natural and anthropogenic SO_2 sources to be identified (section 3.2.3). Long-term averaging would better constrain their existence and magnitude. Finally, the formation of a complete, publicly accessible database of the ν_1 and ν_3 linear retrieval results would allow the wider research community to easily utilise this data in their work.

References

[1] J. C. Walker, A. Dudhia, and E. Carboni, "An effective method for the detection of trace species demonstrated using the MetOp Infrared Atmospheric Sounding Interferometer", Atmospheric Measurement Techniques **4**, 1567–1580 (2011).

[2] E. I. Gordeev and O. A. Girina, "Volcanoes and their hazard to aviation", Herald of the Russian Academy of Sciences **84**, 1–8 (2014).

[3] IATA, *IATA economic briefing: the impact of Eyjafjallajökull volcanic ash plume*, (2010) https://www.iata.org/en/iata-repository/publications/economic-reports/impact-of-ash-plume/ (visited on Feb. 1, 2024).

[4] C. Horwell and P. Baxter, "The respiratory health hazards of volcanic ash: a review for volcanic risk mitigation", Bulletin of Volcanology **69**, 1–24 (2006).

[5] M. R. Rampino, S. Self, and R. B. Stothers, "Volcanic winters", Annual Review of Earth and Planetary Sciences **16**, 73–99 (1988).

[6] A. Bernard and W. I. Rose, "The injection of sulfuric acid aerosols in the stratosphere by the El Chichón volcano and its related hazards to the international air traffic", Natural Hazards **3**, 59–67 (1990).

[7] T. M. Sears, G. E. Thomas, E. Carboni, A. J. A. Smith, and R. G. Grainger, "SO_2 as a possible proxy for volcanic ash in aviation hazard avoidance", Journal of Geophysical Research: Atmospheres **118**, 5698–5709 (2013).

[8] H. E. Thomas and A. J. Prata, "Sulphur dioxide as a volcanic ash proxy during the April–May 2010 eruption of Eyjafjallajökull volcano, Iceland", Atmospheric Chemistry and Physics **11**, 6871–6880 (2011).

[9] E. Carboni, R. Grainger, J. Walker, A. Dudhia, and R. Siddans, "A new scheme for sulphur dioxide retrieval from IASI measurements: application to the Eyjafjallajökull eruption of April and May 2010", Atmospheric Chemistry and Physics **12**, 11417–11434 (2012).

[10] J. C. Walker, E. Carboni, A. Dudhia, and R. G. Grainger, "Improved detection of sulphur dioxide in volcanic plumes using satellite-based hyperspectral infrared measurements: application to the Eyjafjallajökull 2010 eruption", Journal of Geophysical Research: Atmospheres **117**, https://doi.org/10.1029/2011JD016810 (2012).

[11] F. Karagulian, L. Clarisse, C. Clerbaux, A. J. Prata, D. Hurtmans, and P. F. Coheur, "Detection of volcanic SO_2, ash, and H_2SO_4 using the Infrared Atmospheric Sounding Interferometer (IASI)", Journal of Geophysical Research: Atmospheres **115**, https://doi.org/10.1029/2009JD012786 (2010).

[12] WMO, *Instrument: IRS*, (2023) https://space.oscar.wmo.int/instruments/view/irs (visited on Feb. 1, 2024).

[13] J. Schmetz, P. Pili, S. Tjemkes, D. Just, J. Kerkmann, S. Rota, and A. Ratier, "An introduction to Meteosat Second Generation (MSG)", Bulletin of the American Meteorological Society **83**, 977–992 (2002).

[14] C. Clerbaux, A. Boynard, L. Clarisse, M. George, J. Hadji-Lazaro, H. Herbin, D. Hurtmans, M. Pommier, A. Razavi, S. Turquety, C. Wespes, and P.-F. Coheur, "Monitoring of atmospheric composition using the thermal infrared IASI/MetOp sounder", Atmospheric Chemistry and Physics **9**, 6041–6054 (2009).

[15] A. Dudhia, "The Reference Forward Model (RFM)", Journal of Quantitative Spectroscopy and Radiative Transfer **186**, Satellite Remote Sensing and Spectroscopy: Joint ACE-Odin Meeting, October 2015, 243–253 (2017).

[16] A. Smith, "Thoughts about covariance", Mar. 2013.

[17] S. Mackie, O. Embury, C. Old, C. J. Merchant, and P. Francis, "Generalized Bayesian cloud detection for satellite imagery. Part 1: technique and validation for night-time imagery over land and sea", International Journal of Remote Sensing **31**, 2573–2594 (2010).

[18] I. Taylor, S. Mackie, and M. Watson, "Investigating the use of the Saharan dust index as a tool for the detection of volcanic ash in SEVIRI imagery", Journal of Volcanology and Geothermal Research **304**, 126–141 (2015).

[19] I. Taylor, personal communication, Mar. 28, 2024.

[20] E. Carboni, R. G. Grainger, T. A. Mather, D. M. Pyle, G. E. Thomas, R. Siddans, A. J. A. Smith, A. Dudhia, M. E. Koukouli, and D. Balis, "The vertical distribution of volcanic SO_2 plumes measured by IASI", Atmospheric Chemistry and Physics **16**, 4343–4367 (2016).

[21] I. Taylor, personal communication, Mar. 7, 2024.

[22] J. K. Jihyo Kim and E. Heo, "Evolution of the international crude oil market mechanism", Geosystem Engineering **16**, 265–274 (2013).

[23] N. I. Kristiansen, A. J. Prata, A. Stohl, and S. A. Carn, "Stratospheric volcanic ash emissions from the 13 February 2014 Kelut eruption", Geophysical Research Letters **42**, 588–596 (2015).

Appendices

A Calculation of Climatological Column Amount

Calculating x_0, the climatological column amount of SO_2, requires the molar concentration of SO_2 as a function of pressure $v(p)$, obtained from an atmospheric sounding. Consider a vertical column of atmosphere of unit area A. Thin horizontal slices of thickness dp will each have some number of SO_2 molecules dN_{SO_2}. Focusing on a single slice at pressure p, the number of air molecules in the slice dN_{air} is related to dN_{SO_2} by:

$$dN_{SO_2} = v(p) \, dN_{air}. \qquad (11)$$

Introducing the mass of an average molecule of air M_{air} and the mass of air within the slice dm_{air}:

$$dN_{SO_2} = v(p) \frac{dm_{air}}{M_{air}} = v(p) \frac{\rho(p) A \, dz}{M_{air}}. \qquad (12)$$

Here $\rho(p)$ is the density of air. Assuming the atmosphere is in hydrostatic balance ($dp = -\rho g \, dz$):

$$\frac{dN_{SO_2}}{A} = \frac{-1}{M_{air} g} v(p) \, dp. \qquad (13)$$

Integrating the expression and dividing by the Dobson Unit conversion factor $D = 2.69 \times 10^{20}$:

$$x_0 = \frac{N_{SO_2}}{AD} = \frac{1}{M_{air} g D} \int_0^{p_{surface}} v(p) \, dp. \qquad (14)$$

This is easily computed using standard integration packages.

B Simultaneous Linear Retrieval Calculations for Multiple Pixels

Total column amounts for M pixels may be calculated simultaneously through a simple extension of the standard linear retrieval calculation described by (2): x is replaced by $\mathbf{x} \in \mathbb{R}^M$ and $\mathbf{y}$ is replaced by a matrix of spectra $\mathbf{Y}' \in \mathbb{R}^{n \times M}$. Simplifying the notation using the gain vector $\mathbf{g}$ gives:

$$\mathbf{x} = x_0 \mathbf{1}^M + \mathbf{g} \left(\mathbf{Y}' - \mathbf{y}_0 \left(\mathbf{1}^M \right)^T \right), \qquad (15)$$

$$\mathbf{g} = \left(\mathbf{k}^T \mathbf{S}_\epsilon^{-1} \mathbf{k} \right)^{-1} \mathbf{k}^T \mathbf{S}_\epsilon^{-1}. \qquad (16)$$

Here $\mathbf{1}^M \in \mathbb{R}^M$ is a vector for which every entry is unity.

C Computational Calculation of Spectral Ensemble Parameters

Equations (17) and (18) show the linearity of the terms $\mathbf{Y}\mathbf{Y}^T$ and $\bar{\mathbf{y}}$, which are used for calculating the covariance matrix in equation (6). This can be exploited, allowing two datasets A and B to be easily combined. Since $N \gg n$, constructing a running total of $\mathbf{Y}\mathbf{Y}^T \in \mathbb{R}^{n \times n}$ rather than forming the much larger $\mathbf{Y} \in \mathbb{R}^{n \times N}$ improves computational efficiency and decreases memory requirements. Calculations of $\mathbf{Y}\mathbf{Y}^T$ and $\bar{\mathbf{y}}$ were gradually updated with a day of data at a time using this method.

$$\left(\mathbf{Y}\mathbf{Y}^T \right)_{A+B} = \left(\mathbf{Y}\mathbf{Y}^T \right)_A + \left(\mathbf{Y}\mathbf{Y}^T \right)_B \qquad (17)$$

$$\bar{\mathbf{y}}_{A+B} = \frac{N_A \bar{\mathbf{y}}_A + N_B \bar{\mathbf{y}}_B}{N_A + N_B} \qquad (18)$$

D Determining an "Optimal Threshold"

The dependence of the TSS metric on the flagging threshold for the Nabro and Kelud case studies is shown in figures 5 and 6. For $w = 0.5$ and 1, scores remain high below a threshold of zero, demonstrating their poor ability to account for random noise. Visual inspection of $w = 2$ showed that the noise content remained too high to prevent significant numbers of false detections. The choice $w = 5$ provided a reasonable compromise, though larger values could be chosen if the noise content needed to be reduced further.
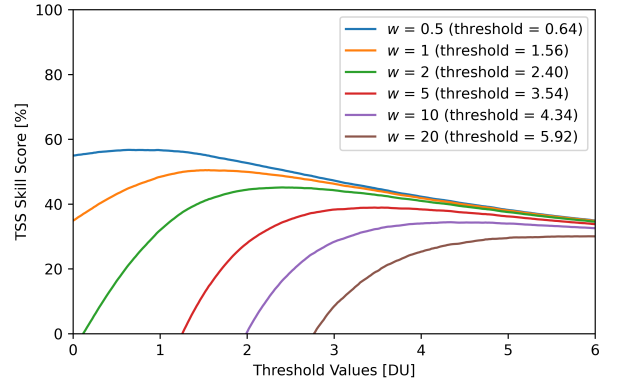

Figure 5: TSS as a function of flagging threshold, applied to data from the first three days of the Nabro 2011 eruption. Each line has a different weighting parameter w, with the threshold that maximises the TSS metric given in parentheses within the legend.
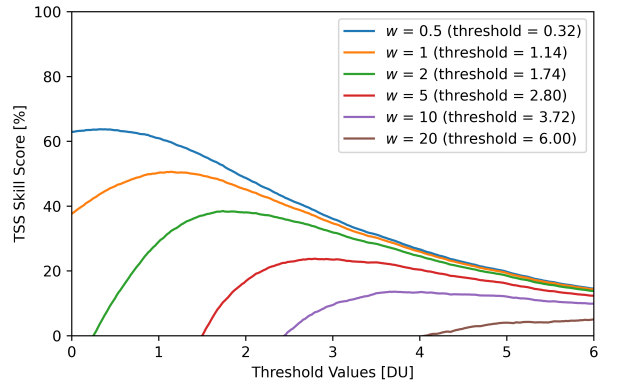

Figure 6: The same as figure 5 but for data from the first three days of the Kelud 2014 eruption.